International Journal of Nanomedicine

Dovepress
open access to scientific and medical research

Open Access Full Text Article

ORIGINAL RESEARCH

Multifunctional Hf/Mn-TCPP Metal-Organic Framework Nanoparticles for Triple-Modality Imaging-Guided PTT/RT Synergistic Cancer Therapy

This article was published in the following Dove Press journal:
International Journal of Nanomedicine

Jianfeng Bao[1,2]
Xiangyang Zu[2]
Xiao Wang[1]
Jinghua Li[2]
Dandan Fan[3]
Yupeng Shi[1]
Qingchun Xia[4]
Jingliang Cheng[1]

[1]Functional Magnetic Resonance and Molecular Imaging Key Laboratory of Henan Province, Department of Magnetic Resonance Imaging, The First Affiliated Hospital of Zhengzhou University, Zhengzhou University, Zhengzhou, Henan, People's Republic of China; [2]College of Medical Technology and Engineering, Henan University of Science and Technology, Luoyang, Henan, People's Republic of China; [3]Henan Institute of Medical and Pharmaceutical Sciences, Zhengzhou University, Zhengzhou, Henan, People's Republic of China; [4]Henan Key Laboratory of Boron Chemistry and Advanced Energy Materials, School of Chemistry and Chemical Engineering, Henan Normal University, Xinxiang, Henan, People's Republic of China

Correspondence: Jingliang Cheng
The First Affiliated Hospital of Zhengzhou University, Zhengzhou University, Zhengzhou, Henan, People's Republic of China
Tel +86-13603863860
Fax +86-37166964992
Email cjr.chjl@vip.163.com

Qingchun Xia
Henan Normal University, Xinxiang, Henan, People's Republic of China
Tel +86-13353679807
Fax +86-3733329030
Email xiaqingchun@htu.edu.cn

Background: Recent studies have validated and confirmed the great potential of nanoscale metal-organic framework (NMOF) in the biomedical field, especially in improving the efficiency of cancer diagnosis and therapy. However, most previous studies only utilized either the metal cluster or the organic ligand of the NMOF for cancer treatments and merely reported limited theranostic functions, which may not be optimized. As a highly designable and easily functionalized material, prospective rational design offers a powerful way to extract the maximum benefit from NMOF for cancer theranostic applications.

Materials and Methods: A NMOF based on hafnium (Hf) cluster and Mn(III)-porphyrin ligand was rational designed and synthesized as a high-performance multifunctional theranostic agent. The folic acid (FA) was modified on the NMOF surface to enhance the cancer targeting efficacy. The proposed "all-in-one" FA-Hf-Mn-NMOF (fHMNM) was characterized and identified using various analytical techniques. Then, in vitro and in vivo studies were performed to further explore the effects of fHMNM both as the magnetic resonance imaging (MRI)/computed tomography (CT)/photoacoustic imaging (PAI) contrast agent and as the photothermal therapy (PTT)/radiotherapy (RT) agent.

Results: A tumour targeting multifunctional fHMNM was successfully synthesized with high performance for MRI/CT/PAI enhancements and image-guided PTT/RT synergistic therapy properties. Compared with the current clinical CT and MR contrast agents, the X-ray attenuation and T_1 relaxation rate of this integrated nanosystem increased 1.7-fold and 3–5-fold, respectively. More importantly, the catalase-like Mn(III)-porphyrin ligand can decompose H_2O_2 into O_2 in tumour microenvironments to improve the synergistic treatment efficiency of PTT and RT. Significant tumour growth inhibition was achieved in mouse cancer models without obvious damage to the other organs.

Conclusion: This work highlights the potential of fHMNM as an easily designable material for biomedical applications, could be an effective tool for in vivo detection and subsequent treatment of tumour.

Keywords: metal-organic framework, theranostics, multimodality imaging, radiotherapy, photothermal therapy

Introduction

Non-invasive diagnostic and therapeutic approaches have been extensively studied for clinical applications. As an imaging diagnostic strategy, ideal medical imaging modalities should provide anatomical, physiological, and molecular information.

submit your manuscript | www.dovepress.com
DovePress
http://doi.org/10.2147/IJN.S267321

The absence of these modalities has driven the development of multimodal imaging, which has become a popular topic and led to the development of imaging technology. If the imaging information is used to guide the non-invasive therapy, the distribution and evolution of the tumour/drug can be seen through time and position resolution patterns, thus improving the efficiency and safety of treatment. Quantum dots and inorganic nanoparticles have been successfully designed and synthesized for multimodal imaging through the integration of various imaging modality agents, but they have biotoxicity and complex preparation procedures. Scientists and clinicians still desire the development of new multimodal image-guided treatment platforms.

Metal-organic framework (MOF) materials are porous materials with basic units of organic linkers and inorganic metal clusters.[1] Due to the designable structures, adequate porosity and easy modification of the metal clusters and organic linkers, MOF materials have shown advances in many fields, such as gas storage and separation, catalysis, sensing, biomedicine and the energy industry.[2–6] Apart from the bulk phase, nanoscale MOFs (NMOFs) have attracted support from researchers[7,8] for their designable multiple elements, porous architecture and good biocompatibility; this is especially true for biomaterials scientists in recent years.[9–12] For example, a series of studies on NMOFs for enhancing photodynamic therapy (PDT), radiotherapy, chemotherapy and immunotherapy were performed by Lin's group,[13–16] and various high-efficiency NMOFs were designed, synthesized and applied for cancer treatments. Wang et al reported a multifunctional Mn-Co-based NMOF that can catalyse tumour endogenous H_2O_2 decomposition for O_2 generation to achieve negative MRI-guided PDT.[17] Yin et al successfully covered a thin photostable porphyrin MOF layer on a catalase-like Mn-Fe_2O_4 nanoparticle to persistently provide O_2 from H_2O_2 for efficient MRI-guided enhanced PDT.[18] Cai et al synthesized a biodegradable pluronic F127-coated Cu-based NMOF, which could be almost eliminated from the body in a month, to enhance PDT efficacy.[19] An increasing number of studies have proven that NMOFs are promising candidates for potential biomedical applications.[20–24] All these exciting research reports indicate that NMOFs can be used as a candidate for potential applications in disease diagnosis and treatments.

In the context of imaging diagnosis and subsequent photothermal therapy/radiation therapy (PTT/RT), functional building blocks should be selected to construct MOFs to achieve these purposes. However, to the best of our knowledge, multifunctional NMOF materials for tumour triple-modality enhanced medical imaging for magnetic resonance imaging/computed tomography/photoacoustic imaging (MRI/CT/PAI) and image-guided PTT/RT synergistic therapy are in their early stages with limited reports. Herein, a water-stable NMOF with Hf_6 as clusters and manganese in the centre of the porphyrin linker was designed and synthesized as a multiple functional nanoplatform for enhancing MRI/CT/PAI images and PTT/RT synergistic therapy. The Mn ion has a long electron relaxation time and enables high positive MRI contrast.[25] As a high-Z element, Hf, with high X-ray attenuation, can be used as an efficient X-ray CT contrast agent[26] and RT.[16] Porphyrins and their derivatives have good photophysical properties and have been widely used as photosensitizers for PDT, PTT and PAI.[27] For tumour targeting, folic acid (FA) was directly conjugated to the Hf_6 cluster with the carboxylate end of the folate by coordination.[28] Furthermore, manganese porphyrin with catalase activity enhances RT through the catalytic decomposition of endogenous H_2O_2 to O_2.[29,30] Then, the potential multifunctional characteristics of FA-Hf-Mn-NMOF (fHMNM) were explored both qualitatively and quantitatively in vitro and in vivo.

Materials and Methods

Materials

Unless otherwise indicated, all chemicals and reagents are available from several commercial suppliers. $HfCl_4$, $MnCl_2$, N,N-dimethylformamide were purchased from Aladin Ltd. (Shanghai, China). All cell culture related reagents were purchased from Sangong (ShangHai, China). The folic acid, DAPI, Calcein-AM/PI were purchased J&K Scientific Ltd. Anti-phospho-Histone H2A.X (Ser139) antibody and goat anti-mouse IgG (Cy3) antibody were purchased from Abcam (Cambridge, MA, USA). Hela, 4T1, MCF10A and S180 cell lines were purchased from Cell Bank of Shanghai Institute of Biochemistry and Cell Biology, Chinese Academy of Science (Shanghai, China). A special culture medium for MCF10A was purchased from Procell Life Science & Technology Co. Ltd. (Wuhan, China). Hydrogen peroxide (H_2O_2) and other chemicals were of analytical grade, purchased from Ruijinte Chemical Reagent Co., Ltd (Tianjin, China). All solutions were prepared with

ultrapure water prepared through a Millipore Milli-Q water purification system (Billerica, MA, USA).

Instruments

X-ray diffraction (XRD) studies were performed with dried HMNM/fHMNM nanoparticles from ethanol on a Philips PW3040/00 X'Pert MPD system with 2θ values from 2° to 50°. To explore the stability of the crystal structure, different treatments related to this work were performed on fHMNM, and then XRD and UV-Vis spectra were obtained. The surface morphology images were obtained on a JEOL JSM-5610 LV scanning electron microscope (SEM, Hitachi Corporation, Japan) with an accelerating voltage of 15 kV. Transmission electron microscopy (TEM) images and element mapping results were obtained on a JEM-2100F field-emission electron microscope (JEOL, Japan) with beam energy of 200 keV. The emission spectrum was obtained using a fluorescence spectrometer (FP-6500, Jasco, Japan). FT-IR Tracer-100 (Shimadzu, Japan) was used for the FT-IR studies. The temperature was recorded with an infrared thermal camera (Testo 865, Testo SE & Co. KGaA, Lenzkirch, Germany) and quantified using a commercially available software (Testo Comfort Software Basic 5.0). Oxygen dissolving meter JPSJ-605 (Leici, Shanghai, China) was used to monitor the O_2 generation. Microwave oven (Multiwave Pro, Anton Paar, Graz, Australia) was used for sample preparation. Inductively Coupled Plasma-Optical Emission Spectroscopy (ICP-OES, Optima 2100, Perkin Elmer) was used for determine the metal elements. Fluorescence imaging was obtained on a confocal microscope confocal (Olympus FV3000, Japan). And phantom in vitro fluorescence images were recorded with NightOWL II LB983 Molecular in vivo imaging system (EG and G Berthold, Germany). A 808 nm near infrared (NIR) laser was generated by LWIRL808-8W (Beijing Laserwave Tech. Co., Ltd). The samples were irradiated with X-rays using Precision X-RAD 320 irradiator (PXi, North Branford, Connecticut, USA). The in vitro X-ray attenuation measurement and the in vivo CT enhancement experiments were performed on a 64 channels Siemens SOMATOM Definition Flash Spiral CT scanner at 120 keV and 25 mA. MRI measurements were performed on 0.5 T (Shanghai Niumai Corporation Ration NM120-Analyst), 1.5 T (Siemens Avanto, Siemens, Erlangen, Germany) 3.0 T scanner (Siemens Prisma, Siemens, Erlangen, Germany) and 7.0 T (Varian Associates, Inc., Palo Alto, CA). The in vitro and in vivo PAI studies were performed on a 64 channel multispectral optoacoustic tomographic imaging system (MSOT, iThera Medical, Munich, Germany).

Synthesis of the Manganese Porphyrin Linker and Folic Acid-Conjugated MOF Nanoparticles

First, the organic tetrakis (4-carboxyphenyl) porphyrin (TCPP) linker unit was successfully synthesized by direct co-condensation, as shown in Figure 1A. Then, manganese was inserted into the centre by a replacement reaction according to a previous study.[31] Then, the hafnium-based manganese porphyrin nanoMOF (HMNM) was synthesized according to a previous study.[32] Briefly, in a round-bottom flask, $HfCl_4$ (0.21 mmol, 67.2 mg), formic acid (20 mL), and Mn-TCPP (0.07 mmol, 61.5 mg) were dissolved in N, N-dimethylformamide (DMF, 60 mL) and then stirred at 65 °C for 48 h. Subsequently, the HMNMs were collected by centrifugation. The product was further washed with DMF and acetone. Finally, the obtained HMNMs were redispersed in water for further experiments. For FA modification, 1 mg of HMNM was dispersed in 5 mL H_2O and fully sonicated for 30 min to achieve a final concentration of 1 mM HMNM in solution, and then 100 μL of 5 mM FA DMSO solution was added into it. After vigorously stirring for 10 min, the mixture was centrifuged (15,000 rpm, 30 min) and washed eight times with DMSO water (v v^{-1}, 1/99) to remove free FA and harvest fHMNM.

In vitro Photothermal Effects and O_2 Generation

Various concentrations (0~500 μg mL^{-1}) of fHMNM in 1 mL water were irradiated for 10 min (808 nm, 1 W cm^{-2}). The contact area of the laser beam in the sample was approximately 0.5 cm^2 and the temperature of the solution was recorded and quantified. The photostability of the fHMNM (100 μg mL^{-1}) was explored by five cycles through irradiation for 10 min and then cooling for another 10 min. 100 μM fHMNM was dispersed in 20 mL water, and then the O_2 dissolved in the water was removed by bubbling nitrogen for 30 min. Then, 10 μL 30% H_2O_2 was added to catalyse the production of O_2, and a dissolved oxygen meter was used to monitor the O_2 generation in real time.

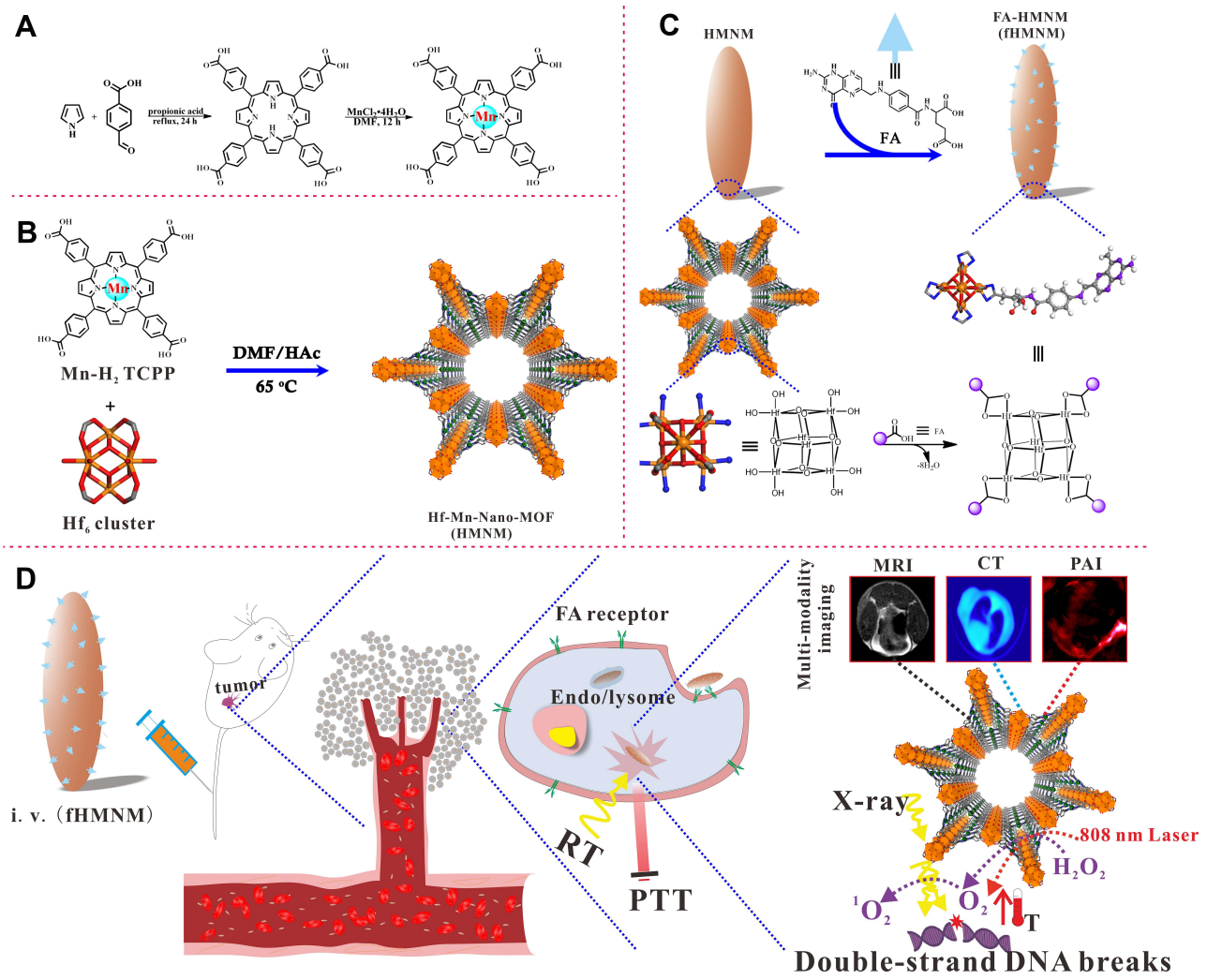

Figure 1 Schematic illustration of the synthetic procedure of fHMNM and as a theranostic agent for in vivo MRI/CT/PAI imaging-guided tumour PTT/RT synergistic therapy. (**A**) Two-step reaction to synthesize the manganese chelate of a tetrapyridinium porphyrin. (**B**) Nanoscale HMNM was synthesized with hafnium as nodes and manganese porphyrin as the ligand. (**C**) HMNM was post-modified with FA by a coordination reaction, and the blue sticks show the available unpaired electrons of the Hf_6 cluster. (**D**) Mechanisms of how the proposed fHMNM performed as a multifunctional agent.

In vitro Cell Uptake, Toxicity, and PTT/RT Synergistic Therapy Assays

Because of the overexpression of FA receptors on the membrane, HeLa cells were used for all in vitro cell experiments.[33] For the cytotoxicity assay, HeLa cells were incubated with various concentrations of HMNM and fHMNM at 37 °C for 12 h to allow sufficient uptake in 96-well culture plates, and then 10 μL of MTT (5 mg mL^{-1}) solution was added to each well. After 4 h of incubation, the absorbance of the cell was measured by a microculture plate reader (Tecan Infinite M200 Pro, Männedorf, Switzerland) at a wavelength of 490 nm. A targeted cell uptake study was performed to test the targeting efficiency. HeLa/MCF10A cells were cultured in 24-well plates at 1×10^5 cells $well^{-1}$ and incubated with different concentrations of HMNM and fHMNM for 12 h. Then, the cells were washed with PBS three times, and 400 μL HNO_3 was added to each well for microwave-assisted digestion for ICP-OES to quantify the amount of hafnium uptake in cells. To test the targeting imaging efficiency, HeLa cells incubated with different concentrations of HMNM and fHMNM for 12 h in a 24-well plate were washed three times and then resuspended in a 1.5 mL centrifuge tube for subsequent in vitro T_1-weighted MRI scan. The PTT/RT synergistic therapy efficiency was explored using both MTT and clonogenic assays. First, HeLa cells were seeded in a 24-well plate and cultured overnight. Then, 20 μM HMNM, fHMNM or PBS was added to the wells and cultured for 12 h. After washing with PBS, the cells were irradiated with 1 W cm^{-2} of an

808 nm NIR laser for 10 min and 4 Gy X-ray independently or jointly, and standard MTT was performed following 4 h of incubation. Additionally, to visualize the live and dead cells, the same procedure was repeated as mentioned above, and the cells were washed gently after different treatments and then stained with calcein-AM/PI for subsequent fluorescence imaging. To assess the long-term therapy efficiency, a clonogenic assay was performed following a previous report.[34] The cells were incubated with 50 μM fHMNM for another 24 h in 6-well plates after PTT with varying laser powers (0, 1, 2, 3, 4 and 5 W cm^{-2}) or RT with varying irradiation doses (0, 2, 4, 6, 8, and 10 Gy). Then, the cells were gently washed with PBS and incubated in fresh culture medium for 10 days to form colonies. The colonies were then fixed with 10% methanol and stained with 0.4% crystal violet. Colonies containing more than 50 cells were counted. The surviving fraction curve was fitted using the clonogenic assay results, and the mean lethal dose D0 was estimated. The DNA double-strand breaks induced by RT were stained by γ-H2AX immunofluorescence following a previous study.[35] Briefly, 4T1 cells were incubated with 20 μM fHMNM and PBS separately in a 24-well plate at 1×10^5 cells $well^{-1}$ for 6 h. After irradiation with 4 Gy X-ray and incubation for another 2 h, the cells were fixed with 4% paraformaldehyde. Then, anti-γ-H2AX was added, and Cy5-conjugated secondary anti-γ-H2AX was added for fluorescence imaging. DAPI was used to label the nuclei. Reactive oxygen species (ROS) generation was probed by 2,7-dichloro-dihydrofluorescein diacetate (DCFH-DA). Cells were cultured in 24-well plates at 1×10^5 cells $well^{-1}$, and then 20 μM fHMNM and DCFH-DA was added to the wells. After incubation with the cells at 37°C for another 6 h, 4 Gy X-ray irradiation was performed.

Tumour-Bearing Mice

All animal experiments were approved by the Institutional Animal Care and Use Committee of Zhengzhou University, China and complied with the Regulations on the Administration of Laboratory Animals promulgated by the Ministry of Science and Technology of China. BALB/c mice were purchased from Beijing Huafukang Bioscience Co. Ltd. (Beijing, China) and were maintained in specified pathogen-free (SPF) environments. S180 tumour cells[36] were obtained from ascitic fluid and subcutaneously implanted in BALC/c mice. For all in vivo experiments, the mice were anesthetized with 1.4% isoflurane during the procedures, and the samples were dispersed in saline and then injected into the mice via the caudal vein.

In vitro and in vivo MRI Experiments

For in vitro MRI, images were obtained on group gradient concentration samples with a maximum of 0.16 mM. In vivo S180 tumour-bearing mice were intravenously injected with 200 μL 2 mg mL^{-1} fHMNM and HMNM, and T_1-weighted MR images were obtained at scheduled time points. The MR signal intensity of the tumour and muscles was recorded for dynamic enhancement analysis. T_1 relaxation times were measured using the inversion recovery (IR) spin-echo method with inversion recovery times varying from 20 to 5120 ms. Since the T_1 relaxation rate is highly dependent on the main magnetic field strength B_0,[37] the relaxation rate measurements were explored and compared on 0.5 T, 1.5 T and 3.0 T human MR scanners and a 7.0 T small animal MR scanner. The most common clinically available magnetic field strengths are 1.5 T and 3.0 T; since the latter has a higher signal-to-noise ratio (SNR) than the former, the in vitro cell and in vivo MRI measurements were performed on a 3.0 T scanner with the following parameters: TR = 800 ms, TE = 20 ms, NEX = 2, FOV = 8×8 cm, matrix = 256×256, and slice thickness = 1 mm.

In vitro and in vivo CT Experiments

For in vitro imaging, CT images were obtained on group gradient concentration samples at a maximum of 80 mg mL^{-1} and fixed by 1% agarose gel. The slice thickness was 0.6 mm, and the in-plane resolution was 100×100 μm. The tumour-bearing mice were injected three times separately with 200 μL of 3 mg mL^{-1} fHMNM in an hour, and CT scans were performed before and after injections at different time points.

In vitro and in vivo Photoacoustic Imaging

First, samples with different concentrations of fHMNM and a maximum concentration of 5 mg mL^{-1} were scanned, and then S180 tumour-bearing mice were injected with 200 μL of 3 mg mL^{-1} fHMNM for PA imaging at different time points. The continuous excitation wavelength was from 750 nm to 950 nm with a 10-nm interval.

In vitro Fluorescence Imaging

Due to its high sensitivity compared to other imaging modalities, the fluorescence imaging technique is very important in current molecular imaging studies.[38,39] Although the manganese element quenches the emission light of porphyrin in fHMNM,[27] as porphyrin is a modifiable material, manganese was easily replaced by

iridium, ruthenium and tin elements, and the fluorescence characteristics were explored preliminarily. The emission spectrum and phantom in vitro fluorescence characteristics were explored preliminarily.

In vivo Photothermal Therapy/ Radiotherapy Assay

To evaluate the in vivo PTT/RT efficiency, twenty S180 tumour-bearing BALC/c mice, which were randomly divided into four groups (n = 5 in each group), were injected with 200 μL of 3 mg mL^{-1} fHMNM or 200 μL saline via the tail vein separately. According to imaging results, after a 24-h injection, the samples were irradiated with 1 W cm^{-2} for 10 min and 4 Gy independently or jointly. The above procedure was repeated 2 days later to enhance the treatments. The body weight and tumour size were measured before and after the treatments.

Histological Analysis

To preliminarily investigate whether the major organs were affected by fHMNM and the corresponding PTT/RT treatments, routine haematoxylin and eosin (H&E) staining was performed on the heart, liver, spleen, lung, kidney and tumour from one mouse in each group just after the second treatments.

Statistical Analysis

Values are expressed as the mean ± standard deviation. Statistical analysis was performed using SPSS 17.0 (SPSS Inc., Chicago, IL). A two-sample *t*-test was used to test the difference between different groups, with $p < 0.05$ (*) and $p < 0.01$ (**) considered statistically significant.

Results and Discussion

Synthesis of FA-Hf-Mn-NMOFs

Figure 1 illustrates how the proposed fHMNM was designed and synthesized and how it works as a multifunctional biomedical nanoplatform. The procedure includes four steps. First, the TCPP linker was synthesized, according to a previously reported method.[32] Then, manganese was inserted into the centre of the porphyrin rings as shown in Figure 1A. The HMNMs were prepared by a one-pot hydrothermal method with Mn-TCPP and hafnium, which are high-Z elements with relatively good biocompatibility, and with formic acid in DMF solution at 65 °C for 48 h as shown in Figure 1B. Due to the easy formation of unusable phases, it is difficult to shrink the MOF particles to nanoparticles. Theoretically, the monomer nucleation step in MOF fabrication can be affected by the reaction temperature and the concentration of each reactant. However, an excess concentration does not seem to shrink MOFs, possibly due to phase impurities. According to a previous study,[20] diluting the whole reaction system to preserve the phase purity strategy was employed in this study to form nanosized MOF particles. To enhance the tumour targeting effect and specificity, FA was conjugated to the Hf_6 nodes, as shown in Figure 1C, through post-synthetic modification following literature protocols.[28] Notably, compared with other Hf node-based MOFs, such as PCN-223 or PCN-221, the hafnium in HMNM based on the PCN-222/MOF-545 structure has more coordination sites, leading to an easier reaction with FA. As shown in Figure 1D, fHMNM could realize the MRI/CT/PAI guided PTT/RT and the Mn-TCPP linker in the fHMNM could modulate tumour hypoxia for effective therapy.

Characterization of FA-Hf-Mn-NMOF

The SEM and TEM images of fHMNM are shown in Figure 2A and B, and the corresponding images of HMNM are shown in Figure S1. The morphology of both HMNM and fHMNM was consistent with previous studies.[20,40] The high-resolution TEM image shown in Figure 2C displays regular lattice fringes. The nanoparticles were confirmed to have a uniform spindle-like shape measuring approximately 32.3 nm along the short axis and 93.4 nm along the long axis by TEM observations (Figure S2A and B). In addition, element mapping images determined by energy dispersive spectroscopy (EDS) are shown in Figure 2F to further verify the existence of the hafnium and manganese functional groups, and the homogeneous distribution of Mn and Hf can be clearly identified in fHMNM. It should be mentioned that the diameter of the hollow space is approximately 4 nm and has been proven to load small-molecule medicines, such as doxorubicin, to deliver drugs.[41,42]

To confirm that the FA molecules were conjugated with Hf_6, fHMNM, FA and the supernatant of the last wash from the reaction between FA and Hf-Mn-NMOF were subjected to UV-Vis analysis. As shown in Figure 2D, fHMNM shows a combined absorption spectrum with NMOF at 420 nm and 490 nm and with FA at 280 nm and 350 nm. After eight washes, no obvious absorption was observed. The UV-Vis results demonstrated that the FA molecules were successfully modified on fHMNM, and

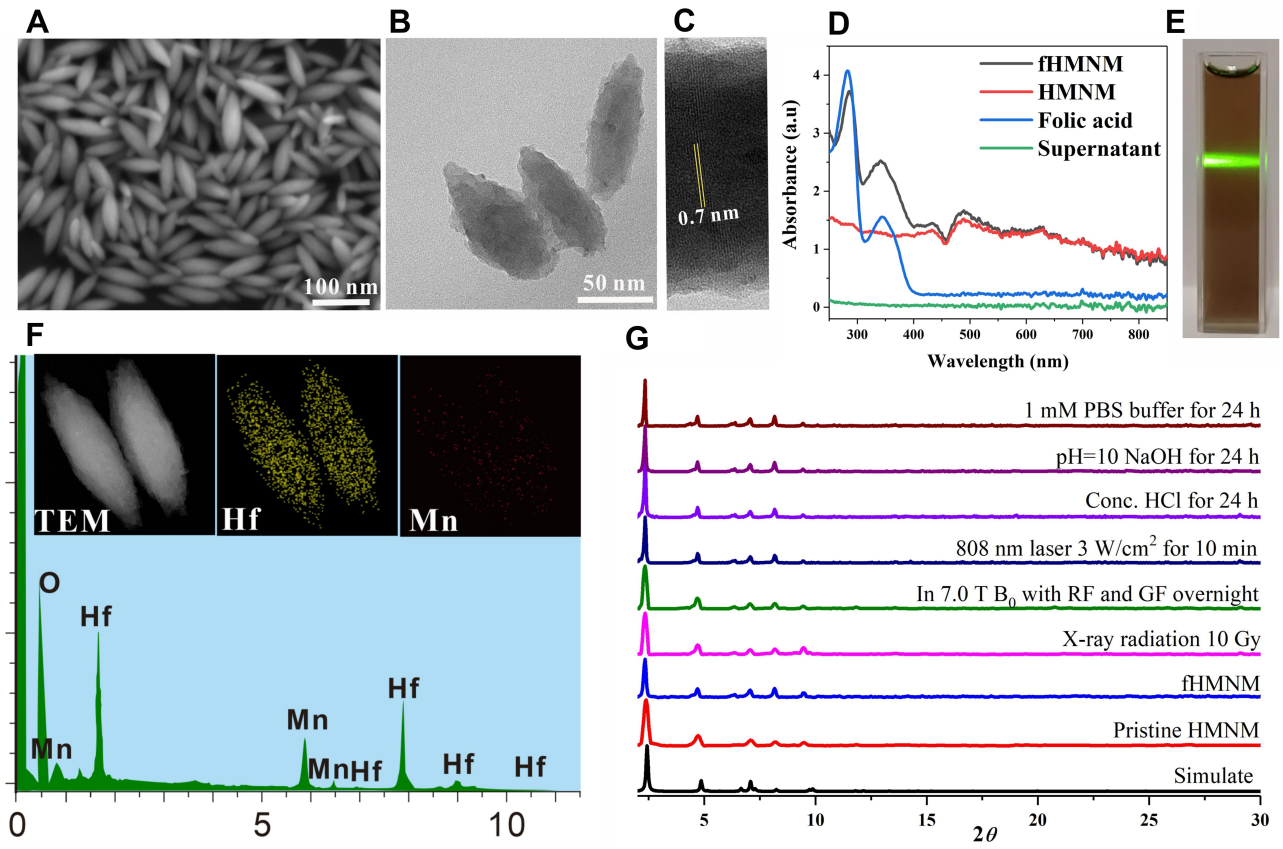

Figure 2 Characterization of the main physicochemical properties of the proposed fHMNM. (**A**) and (**B**) are SEM and TEM images of fHMNM, respectively. (**C**) HR-TEM image of the local area of a single fHMNM. (**D**) UV-Vis absorption spectra of FHMNM, NMOF, FA and the supernatant. (**E**) Photograph of aqueous fHMNM. (**F**) EDS elemental mapping of Mn and Hf of fHMNM. (**G**) Powder X-ray results of fHMNM after treatment under different experimental conditions.

the results were similar to those of a former study.[28] Figure 2E shows the Tyndall effect of the fHMNM by shinning a green light laser onto the transparent solution and confirms the good dispersion of the nanoparticles. Moreover, the higher absorption range of fHMNM in the NIR (from 600 to 800 nm) strongly implied that it may have the potential to serve as a PTT/PAI photosensitizer. With increasing FA, more FA is connected to the Hf nodes; different reaction ratios between FA and hafnium were explored, and the results are shown in Figure S3.The structure of as-synthesized fHMNM was further confirmed by FT-IR, From the FT-IR spectra comparison between HMNM, FA and fHMNM, it can be found that more absorption peaks from FA section appear in the resulting fHMNM (Figure S4), indicating that the reaction was carried out.

XRD patterns are considered to be the primary characteristic to identify MOFs.[43,44] On the basis of the XRD observations, the strong and sharp diffraction peaks indicated that the obtained fHMNM had a highly crystalline microstructure. The pattern shown in Figure 2G consisted of the MOF crystallized in space group P6/mmm with pure phases and good stability, in agreement with previous reports.[32] The four diffraction peaks at 2θ = 2.26, 4.72, 7.12 and 9.76 are consistent with previous studies, and the highest peak at 2.26° suggested there was a preferred orientation of the crystallite. Although a similar Zr-MOF has been proven to be very stable even in some extreme situations, to further ensure that the synthesized fHMNM is stable in the following experimental situations in this work, XRD patterns were obtained for fHMNM under different conditions, such as with a high power laser or high magnetic field, as shown in Figure 2G. Since nonobvious changes were found, fHMNM was expected to be stable and safe for biological applications. To further explore whether FA is stable, UV-Vis was studied. As shown in Figure S5, the FA molecules were still conjugated with NMOF after treated in most situations except treated by the Conc. HCl and NaOH (pH 10), which are neither the physiological environment nor the following treatment.

In vitro Photothermal Assays

Since PTT is attracting increasing interest and becoming more widely used for cancer therapy, and since it was encouraging that the proposed fHMNM had significant absorption in the NIR window, the photoinduced thermal characteristics were evaluated for in vitro phantoms using a 808 nm wavelength lasers. Further in vitro assays of the photothermal properties were performed. As shown in Figure 3A, under continuous irradiation with 1 W cm^{-2}808 nm lasers, dramatic temperature increases were recorded for fHMNM solutions. The photothermal behaviours of the increasing temperature rates and the steady-state temperature are dependent on concentration and irradiation time. As shown in Figure 3B, a higher laser power leads to more rapid thermal effects and a higher final steady-state temperature. A photostable assay of fHMNM was performed, and as shown in Figure 3C, fHMNM retains a robust photothermal conversion after five irradiation-cooling cycles. In addition, IR thermal images were obtained, as shown in Figure 3D, to intuitively monitor and compare the photothermal effects between the fHMNM solution and saline. Therefore, the proposed fHMNM holds great potential as a promising candidate for PTT.

In vitro Cell Experiments

For potential biomedical applications, the in vitro cytotoxicity of fHMNM was first assessed by standard MTT protocols using HeLa cell lines. As shown in Figure S6, the cell viability remained above 90% even after

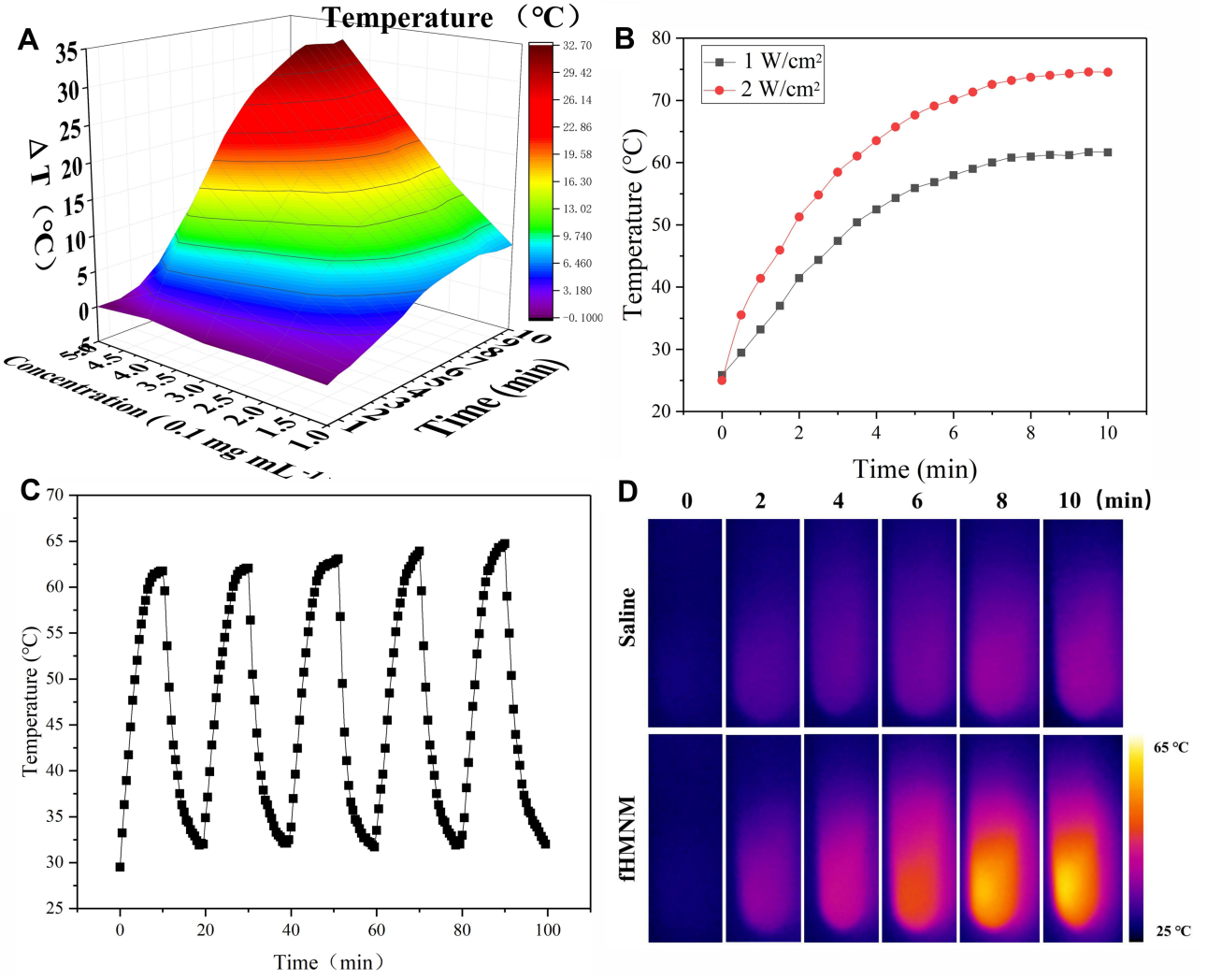

Figure 3 Photothermal characterization of fHMNM. (**A**) Temperature difference diagram with different concentrations of aqueous dispersions of fHMNM and irradiation duration with 808 nm laser irradiation (1 W cm^{-2}). (**B**) The temperature increase curve of fHMNM with different irradiation powers of the 808 nm laser. (**C**) Curve of the photothermal-cooling cycle. (**D**) Infrared thermal images of fHMNM aqueous dispersions with different irradiation times with the 808 nm laser.

incubation with 100 μM fHMNM or HMNM. With increasing concentration, the average cell viability decreased slightly, but no significant cytotoxicity was observed in this study, suggesting that the obtained nanoparticles were biocompatible causing significant cytotoxicity.

As mentioned above, since fHMNM has broad and intense absorption spectra in the NIR window and has high-Z element as nodes, the proposed nanoparticles have the potential to be used for PTT/RT synergistic tumour therapy. To demonstrate the synergistic effects of fHMNM, PTT and RT were applied independently or jointly. The therapeutic effects on cells can be directly seen in Figure 4A. The living cells are green, and the dead cells are red by calcein-AM/PI staining. Almost all of the cells incubated with PBS that experienced either PTT or RT were alive, and unsatisfactory levels of death were found even with combined therapy. For the incubated groups of samples, significantly more cell death was observed in the combined therapy groups than in any other group. Moreover, cell death was more serious in the fHMNM group than in the HMNM group, which may be caused by FA-mediated increases in intracellular sample concentrations. Next, we evaluated the therapeutic effects upon PTT/RT by clonogenic assay. As shown in Figure 4B and C, compared to that in PBS, it is obvious that the survival fraction dramatically drops after irradiation with different doses/powers after incubation with fHMNM. In addition, a DNA damage assay was performed by an immunofluorescent marker of double-strand DNA breaks, γ-H2AX, to evaluate the DNA damage caused by RT (Figure S7) and the surviving fraction parameters are shown in Table S1. These results suggest that fHMNM has the potential to act as a photothermal sensitizer and work together as a radiosensitizer.

As exhibited in Figure 4D, no apparent cytotoxicity of fHMNM was observed without irradiation. In contrast, markedly higher cytotoxicity of fHMNM was found with irradiation with either PTT or RT. At higher concentrations, cells incubated with fHMNM showed significantly lower viability than that of the HMNM group, as expected. This is because the FA-targeting ligand increased the nanoparticle concentration in cells and then improved the corresponding PTT/RT effects. Importantly, the combination of PTT and RT showed strongly significant cytotoxicity compared with either treatment alone. In addition to the heating and ionization effects, according to previous studies,[16,45] the high cytotoxicity of fHMNM caused by PTT and RT may be attributed to the following reasons: the Mn-TCPP linker in fHMNM decomposes endogenous H_2O_2 to O_2, which prevents the repair of DNA damaged by free radicals through the "oxygen fixation hypothesis";[46] the excited triplet state of the Hf_6 cluster can transfer energy directly to ground-state O_2 to generate singlet oxygen $^1O_2$, which leads to lethal damage to cells by damaging various cell membranes.[47] To confirm the above statements, the ability of fHMNM to catalyse H_2O_2 to produce O_2 in vitro was assessed. As shown in Figure S8, after adding fHMNM to H_2O_2 at room temperature, both the generation of bubbles and an increase in O_2 concentration can be observed immediately. This result is consistent with a previous report,[30] which further verifies the oxygen fixation hypothesis for this work. To study the intracellular mechanism of fHMNM as an X-ray response singlet oxygen $^1O_2$ generation medium, a DCFH-DA staining assay was employed to determine the intracellular ROS levels, as shown in Figure S9. The cells in the control, PBS, fHMNM and X-ray alone groups exhibit weak green fluorescence. In contrast, cells treated with fHMNM with 4 Gy irradiation shows strong green fluorescence. These results demonstrate that the proposed fHMNM serves as an efficient agent to generate O_2 and $^1O_2$, which may be further favoured by RT.

The tumour cell targeting efficiency of fHMNM with increased FA receptors compared with non-FA-mediated HMNM was verified by quantifying the Hf uptake in HeLa and MCF10A cells through ICP-OES analyses. As shown in Figure 4E, the mass of Hf was significantly enriched in the fHMNM-treated HeLa cell group compared with the HMNM-treated group. It should be noted that the Hf contents did not increase with increasing concentrations of nanoparticles from 20 and 40 μM. This may be attributed to the saturated endocytosis state of the cells. Moreover, significant lower Hf content was observed in the healthy non-cancerous cell line MCF10A group, which was incubated with fHMNM, than that in HeLa cell group, These results, together with subsequent PTT and MRI cell data, suggest that the proposed fHMNM can specifically target FA receptor tumour cells through the receptor-mediated pathway.

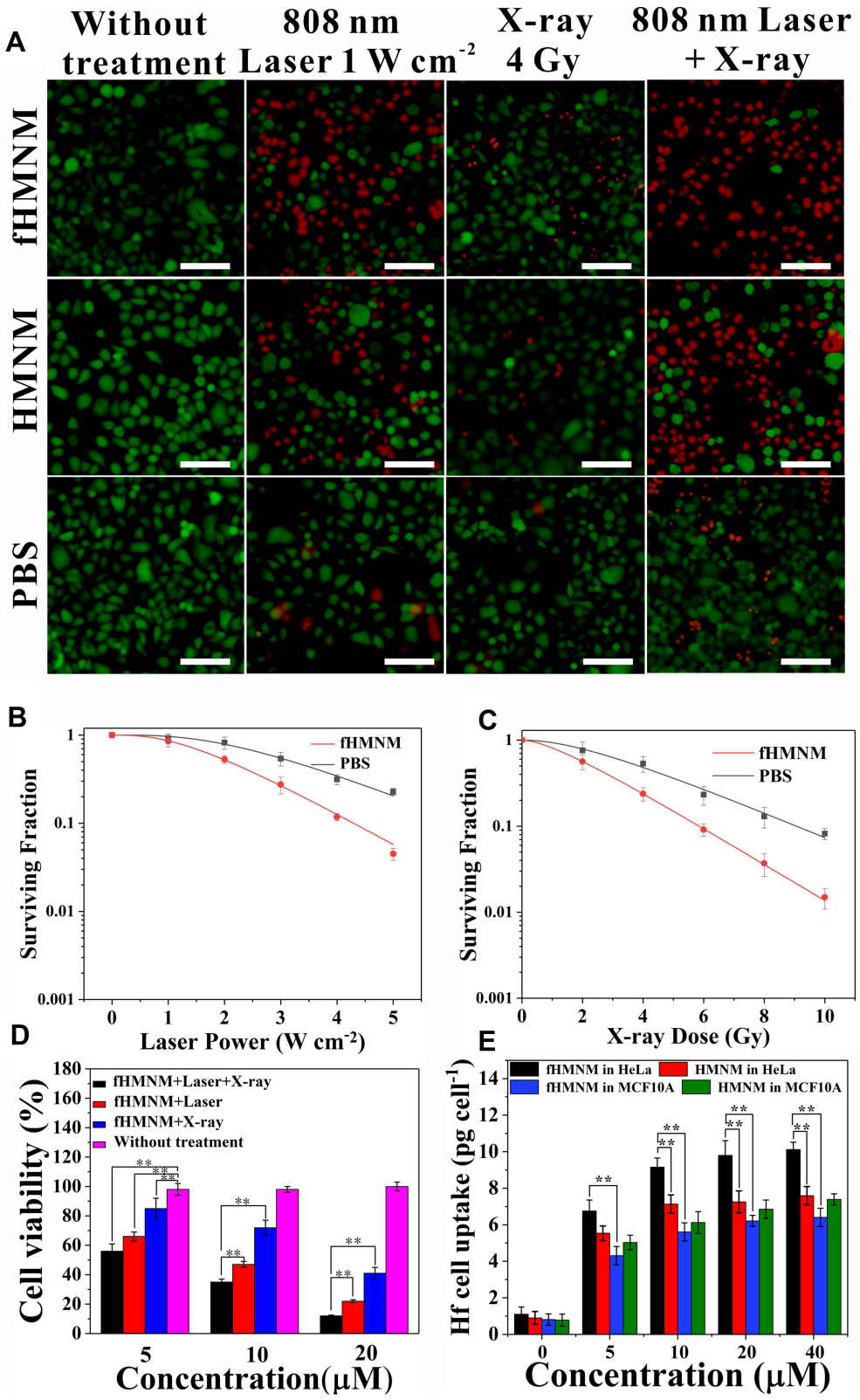

Figure 4 In vitro cell experiments. (**A**) Fluorescence images of calcein-AM- and PI-stained HeLa cells incubated with fHMNM, HMNM and PBS with the 808 nm laser irradiation for 10 min or 4 Gy X-ray irradiation separately or together. The green colour represents living cells, and the red colour represents dead cells. Scale bar: 50 μm. (**B**) Survival curves of HeLa cells treated with 50 μM fHMNM or PBS with 808 nm laser irradiation with varying powers (0, 1, 2, 3, 4 and 5 W cm^{-2}). (**C**) Survival curves of HeLa cells treated with 50 μM fHMNM or PBS with X-ray radiation at varying doses (0, 2, 4, 6, 8 and 10 Gy). (**D**) Cell viability of HeLa cells treated with fHMNM, HMNM and PBS at different concentrations with different treatments (**p < 0.01). (**E**) Comparison of ICP-OES results between the cell uptake of fHMNM and HMNM at various concentrations (n = 3 per group) (**p < 0.01).

In vitro and in vivo Tumour-Targeted MRI Studies

Since manganese is much safer than conventionally used gadolinium, manganese has attracted more attention for MR positive enhancement on T_1-weighted MRI in recent years.[48] Thus, the potential of fHMNM as a MR contrast agent was explored in this work. The T_1 relaxation rates of fHMNM were first measured and compared among HMNM and two widely used clinical MR contrast agents on a 3.0 T scanner. As shown in Figure 5A, the T_1 relaxation rates of both fHMNM (16.75 $mM•S^{-1}$) and HMNM (17.22 $mM•S^{-1}$) are approximately 5 times that of Magnevist and even 3 times that of the macrocyclic contrast agent Gadovist. It is well known that a higher relaxation rate offers better contrast images at the same concentration; thus, fHMNM holds great potential as a high-efficiency MR positive contrast agent. Corresponding T_1-weighted images of the four samples with various concentrations were obtained with the same parameters shown in Figure 5B. Since the relaxation rate is dependent on the B_0 field strength,[37] the T_1 relaxation rate was also measured with different but commonly used B_0 field strengths, as shown in the supporting information (Figure S10). With lower field strength, the T_1 relaxation rate is higher and the T_1 efficiency is more pronounced, but the SNR is much lower.

The extent of the internalization and the targeting imaging efficiency into HeLa cells of fHMNM and HMNM were investigated qualitatively through in vitro cellular MR experiments. Figure 5C shows that the T_1-weighted images show intuitive differences between fHMNM and HMNM at different concentrations. With the same given

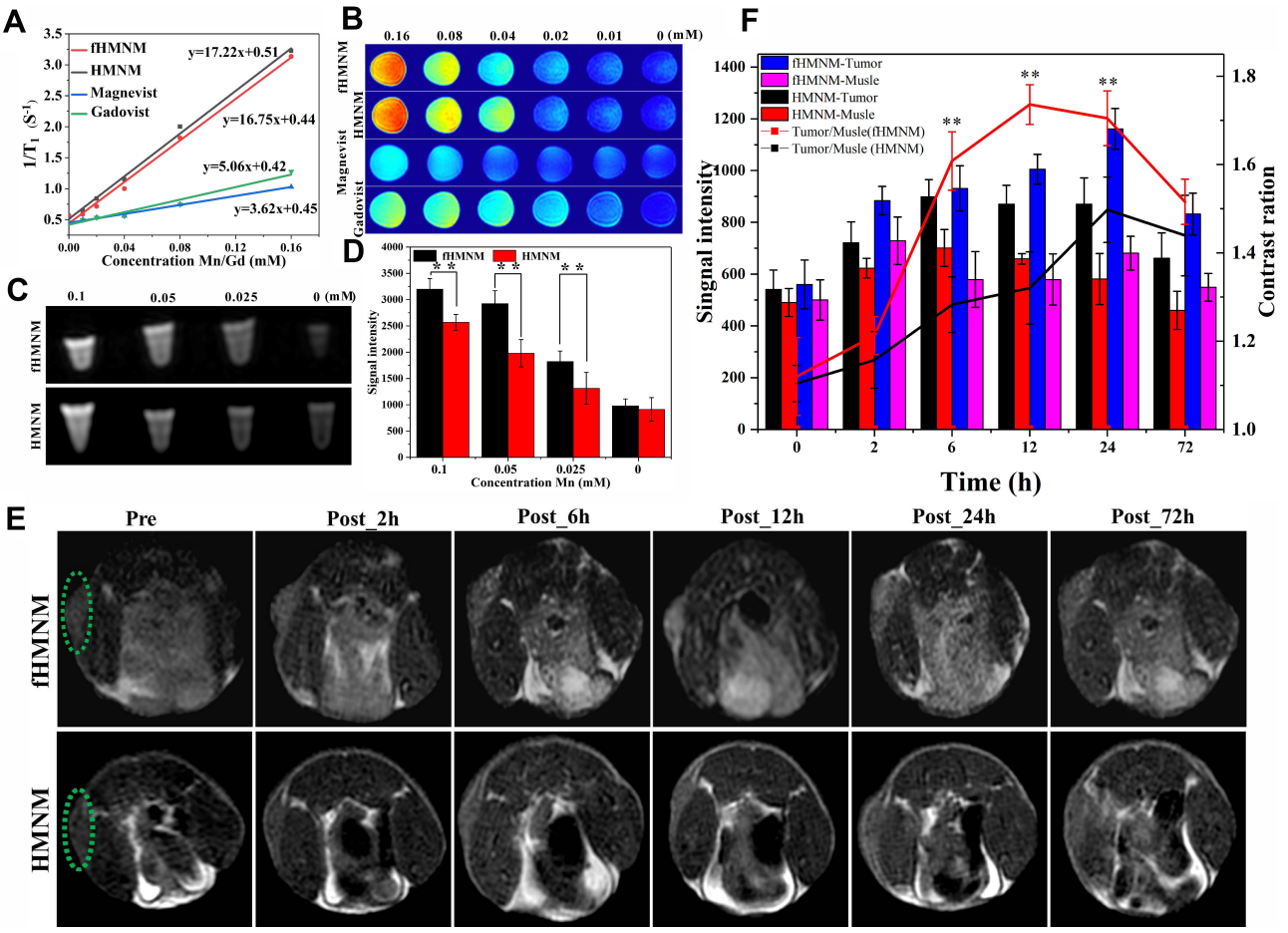

Figure 5 Ex vivo and in vivo studies of fHMNM and HMNM samples as MRI contrast agents. (**A**) T_1 relaxation rates of fHMNM, HMNM, and two commercially available MRI contrast agents (Magnevist and Gadovist) on a human clinical 3.0 T scanner. (**B**) T_1-weighted images of the four samples at different concentrations. (**C**) MR cell experiment comparison among different concentrations of fHMNM and HMNM incubated with cells and (**D**) corresponding MR signal intensity comparison (n = 3 per group). (**E**) In vivo MR experiments comparison between two samples using tumour-bearing mice.The green dotted circles highlighted the tumour regions (n = 3 per group). (**F**) MR signal intensity changes (histogram) and contrast ratio changes between tumour and normal muscle (broken line diagram) over time for fHMNM and HMNM (**p < 0.01), (n = 3 per group).

concentration, the cell uptake fHMNM leads to brighter MR T_1-weighted images than those of HMNM. A quantitative analysis graph is shown in Figure 5D, where fHMNM showed a significantly higher mean MR signal intensity than HMNM. Although with similar T_1 relaxation rates, the in vitro MR results further confirmed that fHMNM possessed tumour targeting MR enhanced imaging abilities.

To examine whether the fHMNM could be used to effectively identify folate-positive tumours in living subjects, in vivo MRI experiments were performed on S180 tumour-bearing mice. Before and after tail vein injection with 200 μL of 2 mg mL^{-1} fHMNM and HMNM, as shown in Figure 5E, mice were scanned to obtain T_1-weighted axial images at different time points, and the solid tumour is denoted by a dashed green circle. It is very clear that the tumour areas have an obvious enhancement in T_1-weighted images with post-injection time for both nanoparticles compared with the pre-injection images. The quantified signal intensity changes in the two samples in tumour and muscle regions were measured and are presented in Figure 5F. Importantly, compared with HMNM, the compromised enhancement is probably attributed to the enhanced permeability and retention (EPR) effect of the NPs. Here, fHMNM shows a noticeably higher MR signal intensity in the tumour region but less enhancement in the muscle region, which results in a better contrast difference between the tumour and muscle (red curve vs black curve in Figure 5F). The in vivo results further suggested that the intravenously injected fHMNM had targeted delivery to the tumour region for effective tumour MR enhanced imaging. It should be noted that the highest tumour MR signal intensity could be achieved at 24 h post-injection of fHMNM, which may be the appropriate time point to perform the subsequent PTT/RT in vivo.

In vitro and in vivo Tumour-Targeted CT and PAI Studies

High-Z elements attenuate X-rays and are thought to increase X-ray irradiation. Due to the high X-ray attenuation.[26,49] Hf (Z = 72) has shown a sensitive CT imaging capability. Thus, to explore the X-ray attenuation property of the developed fHMNM, in vitro CT experiments were conducted with different concentrations of fHMNM phantom, and one clinical CT contrast agent, Iohexol, was used for comparison. As shown in Figure 6A, with increasing concentrations of hafnium or iodine, both samples showed increased CT contrast enhancement, and the increase in CT values was linear with the concentration at the same tube voltage (140 kV). Importantly, the CT attenuation efficiency of fHMNM is 1.7 times higher than that of Iohexol, and the CT phantom images show better contrast efficiency as well, especially at high concentrations. This is ascribed to the fact that the X-ray absorbance of Hf is higher than that of iodine-based CT contrast agents. The potential to use fHMNM for in vivo CT targeting imaging is shown in Figure 6B on a tumour-bearing mouse. Compared to the pre-injection region, the tumour region denoted by a dashed green circle has an obvious enhancement 12 h post-injection, and the subsequent CT attenuation value decreased 72 h post-injection. The mean signal intensity changes with time in the tumour region are recorded and shown in Figure 6C. Quantitative measurements showed that the CT attenuation value increased approximately 2.2-fold at 12 h and 24 h post-injection. The results demonstrated the high CT contrast efficiency of fHMNM, which may have great potential for tumour diagnosis. The results suggest that the proposed fHMNM incorporated with heavy elements can be used for enhancing CT.

PAI is a preclinical imaging modality that combines the advantages of ultrasound imaging and optical imaging, and holds great potential for in vivo deep soft tissue imaging and functional imaging based on the photoacoustic effect.[50] Due to the good and stable photothermal properties of Mn-TCPP, fHMNM may be able to enhance PA imaging. To confirm this hypothesis, in vitro PAI experiments were performed on different concentrations of fHMNM phantom, and then the PAI signal intensity was correlated with the concentration, as shown in Figure 6D. The PAI signal intensity increased with higher fHMNM concentrations. As presented in Figure 6E, in vivo PAI experiments were performed, and axial PA images were acquired at different times for the pre- and post-injection of nanoparticles. Quantitatively, the mean PAI signal intensity of the tumour region continuously increased and reached the highest value at 24 h post-injection as shown in Figure 6F. The subsequent PAI signal intensity decreased at 72 h post-injection. The PAI results proved that the proposed fHMNM may be able to serve as a good PAI contrast agent.

In vivo PTT/RT Synergistic Therapy

Based on the satisfactory in vitro cell therapy results, in vivo PTT/RT was conducted on four parallel groups of

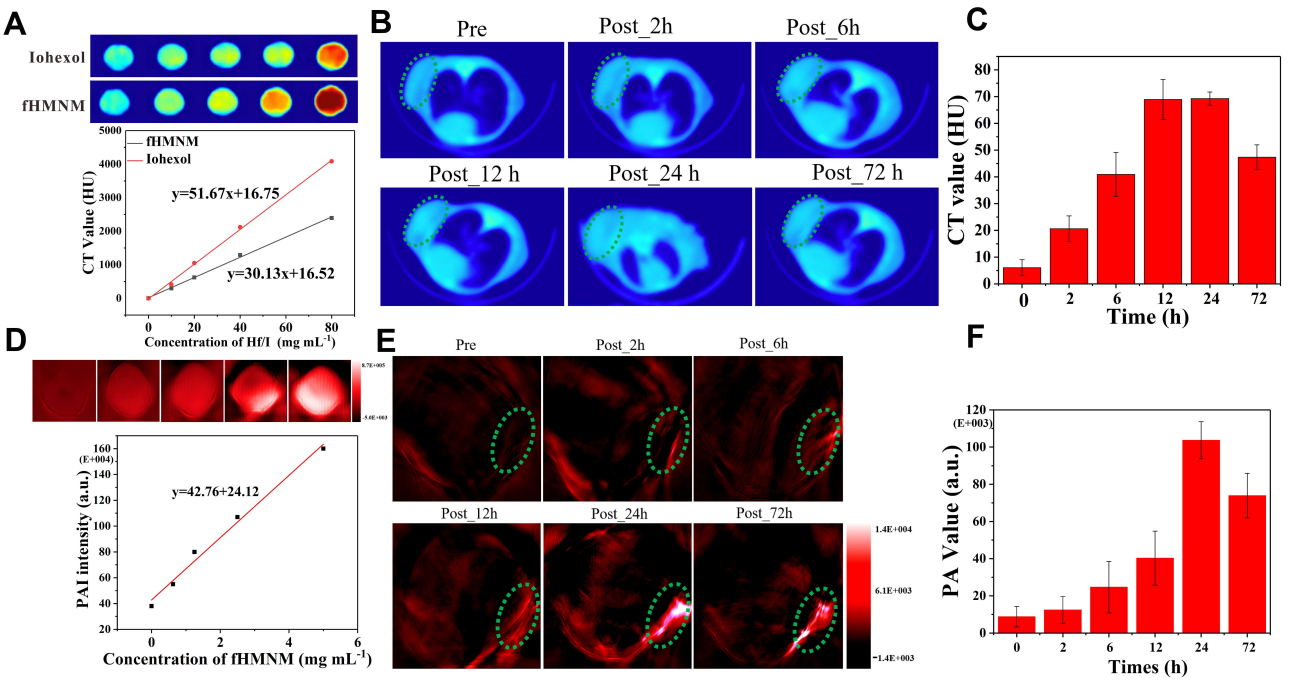

Figure 6 Evaluation of fHMNM as a CT and PAI contrast agent. (**A**) CT images of phantoms and X-ray absorption values of fHMNM (red squares) and Iohexol (black squares) as a function of the concentrations of Hf (red trace) and I (black trace), respectively. (**B**) In vivo axial view of a mouse after fHMNM intravenous injection at different time intervals. The tumour is denoted by a green dashed line ellipse. (**C**) The CT value changes with time in the tumour region. (**D**) PAI images and values of fHMNM with different concentrations. (**E**) PAI images of tumour-bearing mice.The green dotted circles highlighted the tumour regions. (**F**) The PAI signal intensity changes with time in the tumour region.

tumour-bearing mice, as shown in Figure 7D. The experimental group, fHMNM+PTT+RT, was injected with fHMNM, and PTT/RT was applied separately or together for comparisons. Three control groups, fHMNM+RT, fHMNM+PTT and saline, were injected with fHMNM or saline with different treatments. According to the imaging results, the enrichment of fHMNM in the tumour region appears at 24 h after injection. Therefore, the mice were irradiated with 1 W cm^{-2} of an 808 laser for 10 min and 4 Gy X-ray radiation 24 h after the tail vein injection for different groups. It should be noted that since previous studies reported that PTT enhanced the tumour region blood supply and then increases the oxygen concentration,[51] RT was performed immediately after PTT for the experimental group for further synergistic therapy. As shown in Figure 7A, the tumour site shows a much higher temperature for the fHMNM injection than for the saline injection. This is because the FA ligand increases the nanoparticle concentration in the tumour and leads to quicker heating and higher temperatures. Since the body weight loss after medicine administration is always associated with acute medicine toxicity, the body weight was recorded for each mouse after irradiation, and no mouse died in the three groups, as shown in Figure 7B. Compared to the saline group, the body weight of the other three groups did not show significant changes, indicating that fHMNM is safe. The length and width of the tumours were recorded to investigate the in vivo therapy efficiency. After 21 days, the relative tumour volumes ($V\ V_0^{-1}$) for fHMNM+PTT+RT, fHMNM+RT, fHMNM+PTT and saline only were 0.06±0.01, 1.96±0.30, 4.50±0.35 and 7.71 ±0.52, respectively. As shown in Figure 7C, the significant differences in the relative tumour volume among the experimental and control groups indicated that fHMNM could inhibit tumour growth to a significant extent through PTT/RT synergistic therapy. Figure 7D shows representative tumour-bearing mouse pictures after PTT for 21 days and the corresponding final excised tumours are shown in Figure 7E. The tumour histological H&E staining images are shown in Figure 7F to further evaluate the therapeutic effects, which can be seen as obvious cell necrosis and shrinkage for fHMNM+PTT+RT, as expected, but no obvious or only slight necrosis could be found in the other groups. Moreover, as shown in the Table S2, to ensure the practical feasibility of fHMNM for potential clinic application, the hemocompatibility and in vivo toxicity of the proposed nanoparticles was assessed by hemolytic ratio test and analysis.

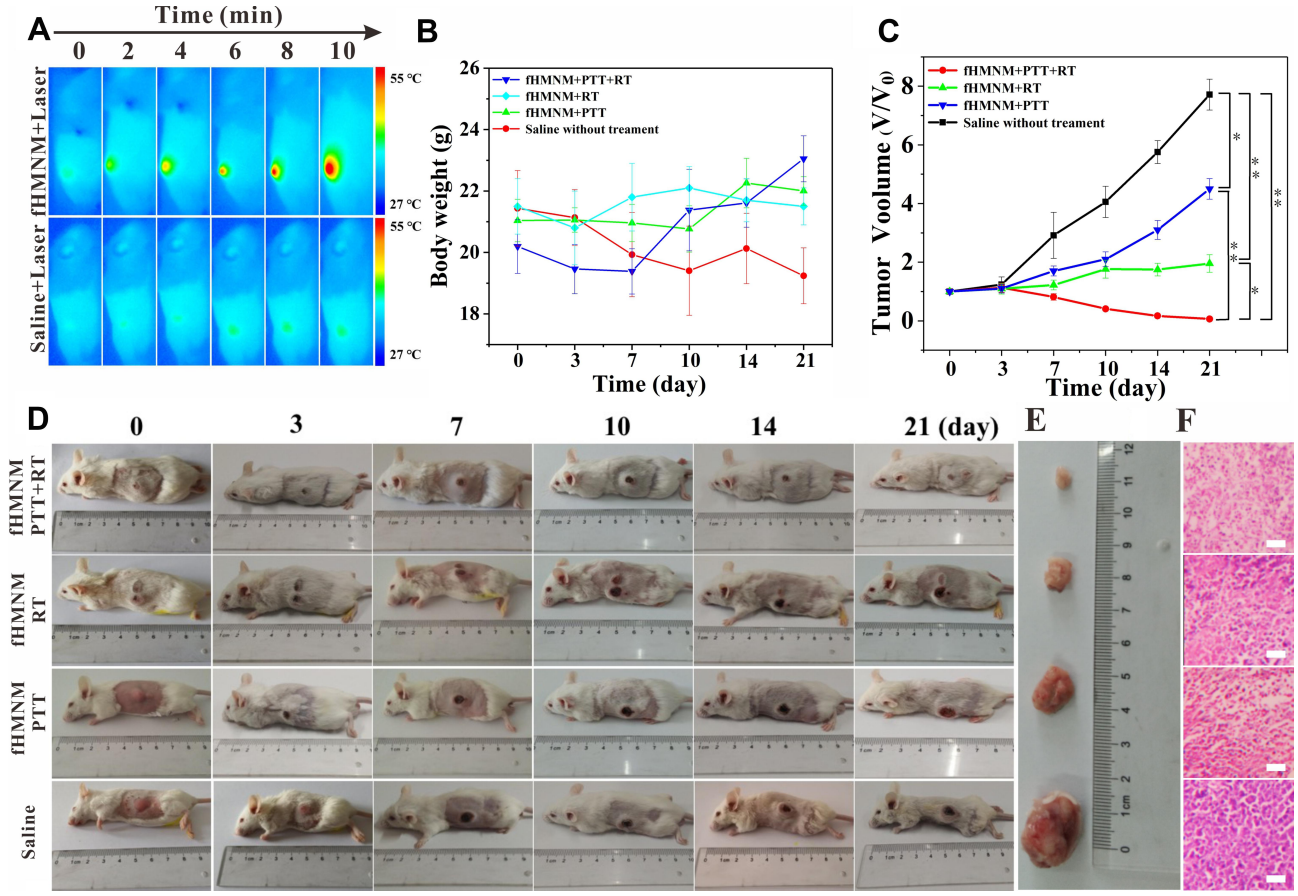

Figure 7 In vivo PTT/RT synergistic therapy efficiency of the proposed fHMNM in tumour-bearing mice. (**A**) NIR thermal images of tumour-bearing mice obtained by an NIR camera. (**B**) Body weight change curves of mice after various treatments, as indicated. (**C**) The relative tumour volume, which was normalized to their initial sizes, and growth curves of the different groups after various treatments (*p < 0.05, **p < 0.01). (**D, E**) Photographs of different therapeutic tumour-bearing mice and corresponding excised tumours at the end of the research (21 days). (**F**) H&E-stained tumour slices collected from mice after various treatments (n = 5 per group), Scale bar: 100 μm.

Histological Analysis

To explore whether fHMNM damages other tissues, the main organs, including the heart, liver, spleen, lung and kidney, were excised, and histological analysis was performed. As shown in Figure S11, no obvious damage was observed for any organ, which preliminarily verified the good biocompatibility of fHMNM.

Preliminary Study on Fluorescence Properties

As the most sensitive imaging modality, fluorescence imaging has been widely used, especially in biomedical fields. Although Mn^{3+}, which was chelated by porphyrin in this study, quenches the fluorescence properties due to spin-orbit coupling perturbations associated with paramagnetic metal ions and electron transfer mechanisms,[52] the fluorescence properties are restored by simply replacing the Mn with other elements, such as iridium (A), ruthenium (B) and tin (C), as shown in Figure S12. Moreover, beyond the recovered fluorescence ability, different new metals in porphyrin may introduce new functions.[53,54]

Conclusion

In this work, a hafnium and manganese-based MOF with FA-functionalized multifunctional theranostic nanoagent, fHMNM, was successfully synthesized and characterized in vitro and in vivo. The agent shows good biocompatibility, targeting MRI/CT/PAI contrast enhanced imaging and imaging-guiding PTT/RT synergistic tumour therapy. More importantly, fHMNM shows superior contrast efficiency for both MRI and CT imaging compared with clinically used agents. The in vitro cellular uptake and cellular targeting MRI assays demonstrated that fHMNM was able to target HeLa cells specifically with higher efficacy than HMNM. Before any nanomedicine can be clinically applied, much more work is needed than this pilot study, such as nephrogenic systemic fibrosis. This

future work is much more relevant for the proposed fHMNM-like nanoparticles with longer circulation and residences than those used in this study. In conclusion, this is the first report detailing the excellent advantages of these NMOFs, and the in vitro and in vivo results demonstrated that fHMNM holds great clinical application potential for targeting the enhancement of MRI/CT/PAT imaging modalities and PTT/RT synergistic treatments of cancer.

Abbreviations

MOF, metal-organic framework; NMOFs, nanoscale metal-organic frameworks; MRI, magnetic resonance imaging; CT, computed tomography; PAI, photoacoustic imaging; PTT, photothermal therapy; PDT, photodynamic therapy; RT, radiotherapy; PCP, porous coordination polymers; FA, folic acid; FA-Hf-Mn-NMOF, fHMNM; TCPP, tetrakis (4-carboxyphenyl) porphyrin; EDS, energy dispersive spectroscopy; EPR, enhanced permeability and retention; SNR, signal-to-noise ratio.

Acknowledgments

This study was supported by the National Natural Science Foundation of China (No. 81601470, No. 21801068, and No. 81901808), the Key Specialized Research and Development Breakthrough of Henan Province (No. 21010035).

Disclosure

The authors report no conflicts of interest in this work.

References

1. Zhou H-C, Long JR, Yaghi OM. Introduction to metal–organic frameworks. *Chem Rev*. 2012;112(2):673–674. doi:10.1021/cr300014x
2. James SL. Metal-organic frameworks. *Chem Soc Rev*. 2003;32(5):276–288. doi:10.1039/B200393G
3. Czaja AU, Trukhan N, Müller U. Industrial applications of metal–organic frameworks. *Chem Soc Rev*. 2009;38(5):1284–1293. doi:10.1039/B804680H
4. Li B, Wen H-M, Cui Y, et al. Emerging multifunctional metal–organic framework materials. *Adv Mater*. 2016;28(40):8819–8860. doi:10.1002/adma.201601133
5. Kalmutzki MJ, Diercks CS, Yaghi OM. Metal–organic frameworks for water harvesting from air. *Adv Mater*. 2018;30(37):1704304. doi:10.1002/adma.201704304
6. Ding M, Flaig R, Jiang H-L, et al. Carbon capture and conversion using metal–organic frameworks and MOF-based materials. *Chem Soc Rev*. 2019;48. doi:10.1039/C8CS00829A
7. Dang S, Zhu Q-L, Xu Q. Nanomaterials derived from metal–organic frameworks. *Nat Rev Mater*. 2017;3(1):17075. doi:10.1038/natrevmats.2017.75
8. Wang S, McGuirk CM, d'Aquino A, et al. Metal–organic framework nanoparticles. *Adv Mater*. 2018;30(37):1800202. doi:10.1002/adma.201800202
9. Cai W, Wang J, Chu C, et al. Metal–organic framework-based stimuli-responsive systems for drug delivery. *Adv Sci*. 2019;6(1):1801526. doi:10.1002/advs.201801526
10. Zhang K, Meng X, Cao Y, et al. Metal–organic framework nanoshuttle for synergistic photodynamic and low-temperature photothermal therapy. *Adv Funct Mater*. 2018;28(42):1804634. doi:10.1002/adfm.201804634
11. Liu J-N, Bu W, Shi J. Chemical design and synthesis of functionalized probes for imaging and treating tumor hypoxia. *Chem Rev*. 2017;117(9):6160–6224. doi:10.1021/acs.chemrev.6b00525
12. Chang J, Lv W, Li Q, et al. One-step synthesis of methylene blue-encapsulated zeolitic imidazolate framework for dual-signal fluorescent and homogeneous electrochemical biosensing. *Anal Chem*. 2020;92(13):8959–8964. doi:10.1021/acs.analchem.0c00952
13. Ni K, Lan G, Veroneau SS, et al. Nanoscale metal-organic frameworks for mitochondria-targeted radiotherapy-radiodynamic therapy. *Nat Commun*. 2018;9(1):4321. doi:10.1038/s41467-018-06655-7
14. Duan X, Chan C, Lin W. Nanoparticle-mediated immunogenic cell death enables and potentiates cancer immunotherapy. *Angew Chem Int Ed*. 2019;58(3):670–680. doi:10.1002/anie.201804882
15. Lan G, Ni K, Veroneau SS, et al. Nanoscale metal–organic layers for radiotherapy–radiodynamic therapy. *J Am Chem Soc*. 2018;140(49):16971–16975. doi:10.1021/jacs.8b11593
16. Lan G, Ni K, Veroneau SS, et al. Nanoscale metal–organic framework hierarchically combines high-Z components for multifarious radio-enhancement. *J Am Chem Soc*. 2019;141(17):6859–6863. doi:10.1021/jacs.9b03029
17. Wang D, Wu H, Lim WQ, et al. A mesoporous nanoenzyme derived from metal–organic frameworks with endogenous oxygen generation to alleviate tumor hypoxia for significantly enhanced photodynamic therapy. *Adv Mater*. 2019;31(27):1901893. doi:10.1002/adma.201901893
18. Yin S-Y, Song G, Yang Y, et al. Persistent regulation of tumor microenvironment via circulating catalysis of MnFe2O4@metal–organic frameworks for enhanced photodynamic therapy. *Adv Funct Mater*. 2019;29(25):1901417. doi:10.1002/adfm.201901417
19. Cai X, Xie Z, Ding B, et al. Monodispersed copper(I)-based nano metal–organic framework as a biodegradable drug carrier with enhanced photodynamic therapy efficacy. *Adv Sci*. 2019;6(15):1900848. doi:10.1002/advs.201900848
20. Bůžek D, Zelenka J, Ulbrich P, et al. Nanoscaled porphyrinic metal–organic frameworks: photosensitizer delivery systems for photodynamic therapy. *J Mater Chem B*. 2017;5(9):1815–1821. doi:10.1039/C6TB03230C
21. Pan X, Bai L, Wang H, et al. Metal–organic-framework-derived carbon nanostructure augmented sonodynamic cancer therapy. *Adv Mater*. 2018;30(23):1800180. doi:10.1002/adma.201800180
22. Zhang X-A, Lovejoy KS, Jasanoff A, et al. Water-soluble porphyrins as a dual-function molecular imaging platform for MRI and fluorescence zinc sensing. *Proc Natl Acad Sci*. 2007;104(26):10780–10785. doi:10.1073/pnas.0702393104
23. Shi Hong S, Wu Y, Liu Y, et al. High drug-loading nanomedicines: progress, current status, and prospects. *Int J Nanomedicine*. 2017:124085–124109. doi:10.2147/IJN.S132780
24. Chang J, Wang X, Wang J, et al. Nucleic acid-functionalized metal–organic framework-based homogeneous electrochemical biosensor for simultaneous detection of multiple tumor biomarkers. *Anal Chem*. 2019;91(5):3604–3610. doi:10.1021/acs.analchem.8b05599
25. Cai X, Zhu Q, Zeng Y, et al. Manganese oxide nanoparticles as MRI contrast agents in tumor multimodal imaging and therapy. *Int J Nanomedicine*. 2019;148321–8344. doi:10.2147/IJN.S218085
26. Berger M, Bauser M, Frenzel T, et al. Hafnium-based contrast agents for X-ray computed tomography. *Inorg Chem*. 2017;56(10):5757–5761. doi:10.1021/acs.inorgchem.7b00359

27. MacDonald TD, Liu TW, Zheng G. An MRI-sensitive, non-photobleachable porphysome photothermal agent. *Angew Chem Int Ed*. 2014;53(27):6956–6959. doi:10.1002/anie.201400133
28. Park J, Jiang Q, Feng D, et al. Size-controlled synthesis of porphyrinic metal–organic framework and functionalization for targeted photodynamic therapy. *J Am Chem Soc*. 2016;138(10):3518–3525. doi:10.1021/jacs.6b00007
29. Naruta Y, Maruyama K. High oxygen-evolving activity of rigidly linked manganese(III) porphyrin dimers. A functional model of manganese catalase. *J Am Chem Soc*. 1991;113(9):3595–3596. doi:10.1021/ja00009a058
30. Chen Y, Zhong H, Wang J, et al. Catalase-like metal–organic framework nanoparticles to enhance radiotherapy in hypoxic cancer and prevent cancer recurrence. *Chem Sci*. 2019;10(22):5773–5778. doi:10.1039/C9SC00747D
31. Farokhi A, Hosseini-Monfared H. A recyclable Mn–porphyrin catalyst for enantioselective epoxidation of unfunctionalized olefins using molecular dioxygen. *New J Chem*. 2016;40(6):5032–5043. doi:10.1039/C6NJ00808A
32. Feng D, Gu Z-Y, Li J-R, et al. Zirconium-metalloporphyrin PCN-222: mesoporous metal-organic frameworks with ultrahigh stability as biomimetic catalysts. *Angew Chem Int Ed*. 2012;51 (41):10307–10310. doi:10.1002/anie.201204475
33. Siwowska K, Schmid RM, Cohrs S, et al. Folate receptor-positive gynecological cancer cells: in vitro and in vivo characterization. *Pharmaceuticals*. 2017;10(4):72. doi:10.3390/ph10030072
34. Xu X, Chong Y, Liu X, et al. Multifunctional nanotheranostic gold nanocages for photoacoustic imaging guided radio/photodynamic/photothermal synergistic therapy. *Acta Biomater*. 2019:84328–84338. doi:10.1016/j.actbio.2018.11.043
35. Song G, Liang C, Gong H, et al. Core–shell MnSe@Bi2Se3 fabricated via a cation exchange method as novel nanotheranostics for multimodal imaging and synergistic thermoradiotherapy. *Adv Mater*. 2015;27(40):6110–6117. doi:10.1002/adma.201503006
36. Wang M, Hu H, Sun Y, et al. A pH-sensitive gene delivery system based on folic acid-PEG-chitosan – PAMAM-plasmid DNA complexes for cancer cell targeting. *Biomaterials*. 2013;34 (38):10120–10132. doi:10.1016/j.biomaterials.2013.09.006
37. Rohrer M, Bauer H, Mintorovitch J, Requardt M, Weinmann H-J. Comparison of magnetic properties of MRI contrast media solutions at different magnetic field strengths. *Invest Radiol*. 2005;40 (11):715–724. doi:10.1097/01.rli.0000184756.66360.d3
38. Zhang P, Tian Y, Liu H, et al. In vivo imaging of hepatocellular nitric oxide using a hepatocyte-targeting fluorescent sensor. *Chem Commun*. 2018;54(52):7231–7234. doi:10.1039/C8CC03240H
39. Li H, Lin H, Lv W, et al. Equipment-free and visual detection of multiple biomarkers via an aggregation induced emission luminogen-based paper biosensor. *Biosens Bioelectron*. 2020;165112336. doi:10.1016/j.bios.2020.112336
40. Tian X-T, Cao -P-P, Zhang H, et al. GSH-activated MRI-guided enhanced photodynamic- and chemo-combination therapy with a MnO2-coated porphyrin metal organic framework. *Chem Commun*. 2019;55(44):6241–6244. doi:10.1039/C9CC01957J
41. Zhang H, Tian X-T, Shang Y, et al. Theranostic Mn-porphyrin metal–organic frameworks for magnetic resonance imaging-guided nitric oxide and photothermal synergistic therapy. *ACS Appl Mater Interfaces*. 2018;10(34):28390–28398. doi:10.1021/acsami.8b09680
42. Pander M, Żelichowska A, Bury W. Probing mesoporous Zr-MOF as drug delivery system for carboxylate functionalized molecules. *Polyhedron*. 2018;156131–137. doi:10.1016/j.poly.2018.09.006
43. Biemmi E, Christian S, Stock N, et al. High-throughput screening of synthesis parameters in the formation of the metal-organic frameworks MOF-5 and HKUST-1. *Microporous Mesoporous Mater*. 2009;117(1–2):111–117. doi:10.1016/j.micromeso.2008.06.040
44. Sabo M, Henschel A, Fröde H, et al. Solution infiltration of palladium into MOF-5: synthesis, physisorption and catalytic properties. *J Mater Chem*. 2007;17(36):3827–3832. doi:10.1039/B706432B
45. Alford A, Kozlovskaya V, Xue B, et al. Manganoporphyrin-polyphenol multilayer capsules as radical and Reactive Oxygen Species (ROS) scavengers. *Chem Mater*. 2018;30(2):344–357. doi:10.1021/acs.chemmater.7b03502
46. Robert Grimes D, Partridge M. A mechanistic investigation of the oxygen fixation hypothesis and oxygen enhancement ratio. *Biomed Phys Eng Express*. 2015;1(4):045209. doi:10.1088/2057-1976/1/4/045209
47. Weishaupt KR, Gomer CJ, Dougherty TJ. Identification of singlet oxygen as the cytotoxic agent in photo-inactivation of a murine tumor. *Cancer Res*. 1976;36(7Part 1):2326.
48. Gale EM, Atanasova IP, Blasi F, et al. A manganese alternative to gadolinium for MRI contrast. *J Am Chem Soc*. 2015;137 (49):15548–15557. doi:10.1021/jacs.5b10748
49. deKrafft KE, Boyle WS, Burk LM, et al. Zr- and Hf-based nanoscale metal–organic frameworks as contrast agents for computed tomography. *J Mater Chem*. 2012;22(35):18139–18144. doi:10.1039/C2JM32299D
50. Weber J, Beard PC, Bohndiek SE. Contrast agents for molecular photoacoustic imaging. *Nat Methods*. 2016;13639. doi:10.1038/nmeth.3929
51. Wang S, You Q, Wang J, et al. MSOT/CT/MR imaging-guided and hypoxia-maneuvered oxygen self-supply radiotherapy based on one-pot MnO2-mSiO2@Au nanoparticles. *Nanoscale*. 2019;11 (13):6270–6284. doi:10.1039/C9NR00918C
52. Fudickar W, Zimmermann J, Ruhlmann L, et al. Fluorescence quenching and size selective heterodimerization of a porphyrin adsorbed to gold and embedded in rigid membrane gaps. *J Am Chem Soc*. 1999;121(41):9539–9545. doi:10.1021/ja991738n
53. Zhang Y, Lovell JF. Porphyrins as theranostic agents from prehistoric to modern times. *Theranostics*. 2012;2(9):905–915. doi:10.7150/thno.4908
54. Brothers PJ. *Organometallic Chemistry of Transition Metal Porphyrin Complexes, Adv Organomet Chem*. Academic Press; 2000:223–321.